Chapter 2

Space Borne Observations and Some Analysis Techniques

In this chapter, we briefly describe various space-borne observatories (e.g., Solar Dynamics Observatory *SDO;* ***Interface Region Imaging Spectrograph*** *IRIS),* ***and onboard instruments (e.g., Helioseismic and Magnetic Imager*** *HMI,* ***Atmospheric Imaging Assembly*** *AIA;* ***IRIS Slit-jaw Imager*** *SJI* ***and Spectrograph). Making use of a variety of the observations from these instruments, we have analyzed them to pursue some new scientific studies in this thesis. We also describe the key data analysis techniques utilized in the works, e.g., the image calibration and processing, analysis techniques of magnetogram data, spectral fitting procedure and related diagnostics, Differential Emission Measure (DEM) analysis, time-series wavelet analysis, etc. Finally, we conclude the significance of the analyzed observations and analysis techniques.***

2.1 Introduction

The spectroscopic and imaging observations of the emission lines and continuum radiation in the Ultraviolet (UV) and/or Extreme Ultraviolet (EUV) wavelength range of the electromagnetic spectrum, provide a unique tool to probe the dynamics and properties of various layers of the hot solar atmosphere (e.g., Curdt et al., 2001; Del Zanna & Mason, 2018; Dwivedi, 1993; Hinode Review Team et al., 2019; Tian, 2017; Wilhelm et al., 2007, and references cited there). In addition, the high energy counterparts associated with various dynamical phenomena (e.g., flare, coronal jets, magnetic reconnection and associated energy release) which occur in the localized magnetic environment of the solar atmosphere, can also be studied through the high temperature EUV, soft, and hard X-ray emissions (e.g., Benz, 2017; Chen, 2011; Raouafi et al., 2016; Shibata & Magara, 2011, and references cited there). Therefore, ultraviolet and X-ray emissions together from corona capture a range of the physical phenomena in the hot solar atmosphere. In particular, the most of the UV/EUV emissions are formed above the temperature minimum between the formation temperature 10,000 K to 20 MK in the solar atmosphere (Wilhelm et al., 2004). The high temperature forms the ions of different ionization states, which emit the UV/EUV spectral lines significant for the characterization of the chromosphere, transition region, corona (e.g., Del Zanna & Mason, 2018; Dwivedi, 1993; Mariska, 1992; Wilhelm et al., 2007, and references cited there). These emissions also help in understanding the range of physical processes in the solar atmosphere, e.g., energy and mass transport, waves, jets/plasma flows, large-scale eruptive phenomena like flare and CMEs, magnetic reconnection and associated dynamical plasma processes, etc (e.g., Aschwanden, 2019). Some molecular/atomic lines and the continua originate in cooler regions of the Sun below the temperature minimum between the photosphere and the lower chromosphere, and some of these atomic radiations are sensitive to the magnetic fields at the solar surface allowing to probe them through magnetogram/spectropolarimetric observations (e.g., Lagg et al., 2017;

Leenaarts et al., 2012; Stenflo, 2013, references cited there). Collectively, the magnetic and/or spectropolarimetric, imaging, and spectroscopic observations revealing the coupling of various layers of the solar atmosphere above a certain magnetic region (e.g., sunspots in the active regions; network/internetwork regions in quiet-Sun; coronal hole regions; flux emerging regions, etc) play a vital role in understanding the dynamical physical processes (e.g., waves, flows, eruptions, heating, etc.) in the modern day solar astronomy.

Radiation at UV and X-ray wavelengths are strongly absorbed by the Earth's atmosphere, therefore, they can only be detected with the instruments on sounding rockets and spacecraft operating above its atmosphere (e.g., Brosius et al., 1996; Culhane et al., 2007b; De Pontieu et al., 2014a; Wilhelm et al., 2004, and references cited there). The present thesis outlines novel scientific results related to the understanding of cool plasma flows generated in the upper chromosphere/TR, plasma flow structure at the footpoint of hot loops anchored in the moss regions, and some supersonic plasma flow/jet above a plage region in the quiet Sun. Therefore, the UV/EUV emissions from various ions formed from the chromosphere to the corona are utilized in deriving various scientific results. Moreover, magnetogram observations are also utilized to understand the magnetic field properties of the studied regions of the solar atmosphere. The solar observations are obtained, therefore, from various space-borne observatories, namely, Solar Dynamics Observatory (SDO) and Interface Region Imaging Spectrograph (IRIS). These observations are then analyzed using various techniques to get the physical information. The observational instruments and techniques are, therefore, explained in this chapter. The space-based instruments which are mainly used for the studies in this thesis are Atmospheric Imaging Assembly (AIA)/SDO; Helioseismic and Magnetic Imager (HMI)/SDO; Slit-Jaw Imager (SJI)/IRIS and Spectrograph. The details of these instruments are provided in Sect. 2.2. The methods adopted for different kinds of data analysis in this thesis are mentioned in the Sect. 2.3. In the last section, we make a brief conclusion on the potential role of these instruments and analyzed data in this thesis.

2.2 Space-based Instruments

The works in this thesis is mostly based on imaging and spectral data from space-based instruments. The techniques and principles regarding the working of these telescopes are described below along with a few examples to illustrate the solar observations from these instruments.

2.2.1 Solar Dynamics Observatory (SDO)

SDO (Pesnell et al., 2012) is a NASA′s space mission under Living With Star (LWS) program. It was launched on 11th February 2010 and placed at geo-synchronous orbit. It weighed 3000 kg at the time of launch having dimensions 4.7 m and contains solar arrays of 6.6 m^2 capable of producing 1500 W of power. It started to provide observational data from 1st May 2010 which has potential to investigate the Sun′s magnetic field and physical mechanisms to release magnetic energy into the heliosphere. SDO has three instruments, namely, Extreme ultraviolet Variability Explorer (EVE); Atmospheric Imaging Assembly (AIA); Helioseismic and Magnetic Imager (HMI)) onboard, each dedicated to different scientific investigations. AIA and EVE focus on the energy radiated in the extreme Ultraviolet domain of the wavelength range. HMI, however, measures the variations in the magnetic field and helps us in understanding and measuring the internal motions generating magnetic fields at the surface of the Sun, thus enabling the enhancement of helioseismic and line-of-sight (LOS) magnetic field capabilities. SDO provides high-resolution data mainly focusing its science data regarding eruptive events, flare, and CMEs. The solar images are recorded on CCD containing 4096 × 4096 pixels.

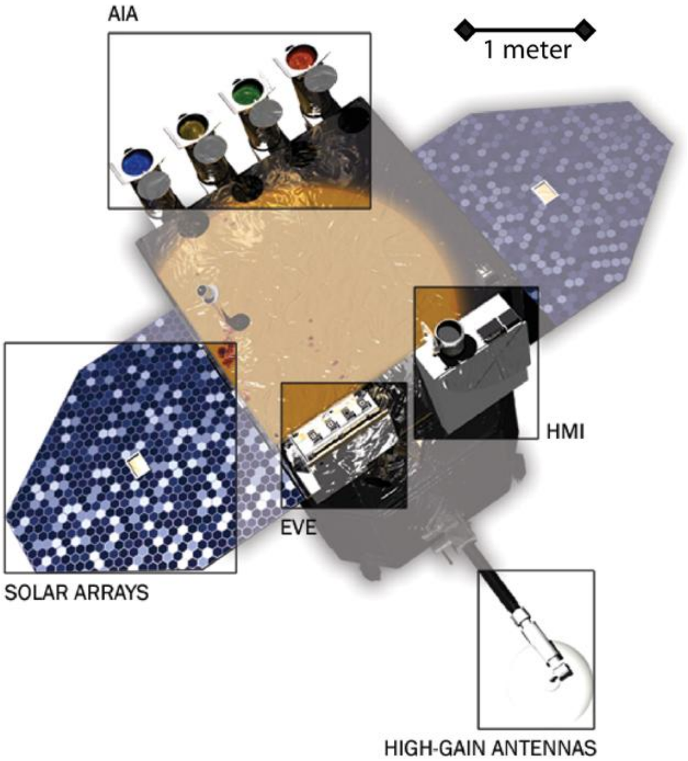

Figure 2.1: Schematic view of the arrangement of different instruments onboard Solar Dynamics Observatory. (Courtesy:-LMSAL, NASA, SDO)

Channel	Primary ion	Region of atmosphere	Char. log T
4500Å	continuum	photosphere	3.7
1700Å	continuum	temperature minimum, photosphere	3.7
304Å	He II	chromosphere, transition region	4.7
1600Å	C IV + cont.	transition region, upper photosphere	5.0
171Å	Fe IX	quiet corona, upper transition region	5.8
193Å	Fe XII , XXIV	corona and hot flare plasma	6.2, 7.3
211Å	Fe XIV	active-region corona	6.3
335Å	Fe XVI	active-region corona	6.4
94Å	Fe XVIII	flaring corona	6.8
131Å	Fe VIII , XXI	transition region, flaring corona	5.6, 7.0

Table 2.1: The primary ions, their formation temperature, and emitted wavelengths as observed by AIA. (Courtesy: Lemen et al., 2012)

Atmospheric Imaging Assembly (AIA)

It is a multi-wavelength imager instrument onboard SDO which provides the full-disk images of the surface and atmosphere of the Sun (Lemen et al., 2012). The images cover a field-of-view of $\approx 41'$ with a two-pixel resolution of 1.2". It consists an array of four Cassegrain 20-cm telescopes for ten different wavelength bands in UV/EUV range. Three of the telescopes have two different EUV bandpasses while the other one has 171 Å on the half and UV broadband coating on the other half. The telescope mirrors are fabricated on Zedour substrates providing low coefficient of thermal expansion. The mirrors are coated with aluminium with an MgF_2 protective overcoat. This combination of multilayer coatings and foil filters helps to isolate the desired spectral bandpasses for each telescope. These narrow wavelength bandpasses thus enable it to provide the images of the corona for seven EUV, two UV, and one visible light band. The filters are centered on specific lines Fe XVIII (94 Å), Fe VIII, XXI (131 Å), Fe IX (171 Å), Fe XII, XXIV (193 Å), Fe XIV (211 Å), He II (304 Å), Fe XVI (335 Å), C IV (near 1600 Å) and nearby continuum (1700 Å) corresponding to different regions characterized by the formation temperature of these ions as described in Table 2.1.

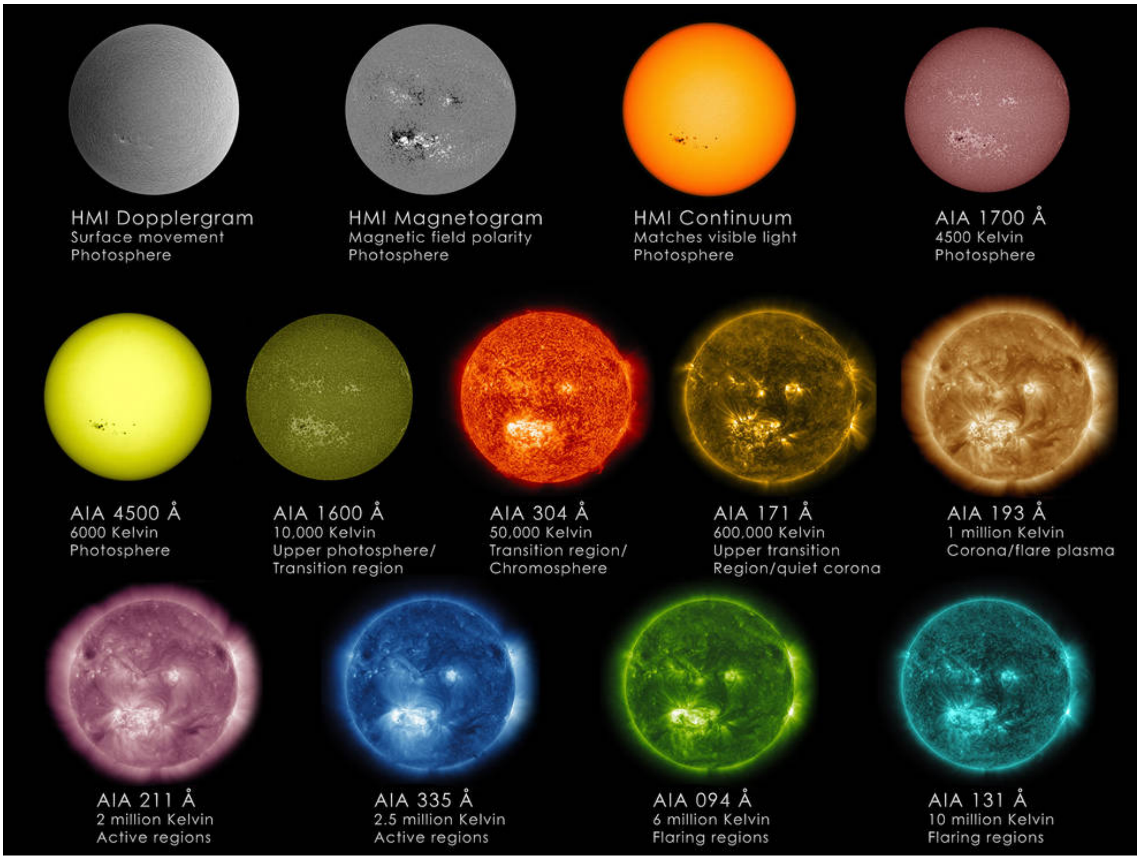

Figure 2.2: Multi-wavelength view of the Sun using AIA and HMI instruments onboard SDO highlighting different features. (Courtesy: NASA/SDO/Goddard Space Flight Center)

This instrument is used to conduct multi-wavelength studies of the dynamics of solar atmosphere. The solar atmospheric activities rely on energy dissipation within the plasma contained in the Sun′s magnetic field. The magnetic field keeps restructuring itself giving rise to massive eruptions, waves and oscillations, confined plasma flows and jets. Therefore, AIA helps us understand the initiation and the evolution of such dynamical processes. It also gives insights into small-scale transients due to its high-spatial resolution. The study of a supersonic plasma flow/jet is studied using multi-filter/multi-temperature imaging observations from AIA (cf., Chapter 6). The plasma conditions at different temperatures have been exploited in our works through AIA imaging observations using its various filters. The instrument holds other broad range of science objectives as well such as coronal heating and irradiance, transient, connections to geospace, coronal seismology. Fig.2.2

shows the full disk images of the Sun in the various wavelength bands of AIA and HMI. The HMI magnetogram shows the magnetic field polarities where white represents positive polarity indicating magnetic fields coming out of the Sun, while black shows the negative polarity indicating magnetic fields going inside. HMI continuum shows the visible light emission highlighting the magnetic field at the sunspots. AIA 1600 Å , 1700 Å , 4500 Å highlight the dark photospheric emission for sunspots and bright emission for plage regions surrounding it. AIA 304 Å corresponds to the upper chromospheric/TR emissions for bright active regions and shows the supergranules in the quiet-Sun region. All other filters correspond to the coronal emissions highlighting coronal activities above the active region and highly energetic eruptive events. This infers that AIA provides co-spatial observations covering from top of the photosphere to the inner corona, thus enabling understanding the Sun's atmospheric coupling.

Fig.2.3 shows a zoomed FOV of an active region observed on 15 February 2011 at 01:45 UT in multi-wavelength channels of AIA. The top row panels are observations from the 131 Å , 94 Å , and 335 Å channels (left to right in sequence) sensitive to the highest temperature plasma present in AR (cf., Table 2.1). The middle row panels are from the 171 Å , 193 Å , and 211 Å channels sensitive to the typical coronal temperatures of a few mega Kelvin (cf., Table 2.1). The bottom row panels are from 1600 Å and 304 Å (left and middle, respectively), which display the cool plasma components present at upper-photospheric, chromospheric, and TR temperatures (cf., Table 2.1). The bottom right corner panel is an HMI line-of-sight magnetogram showing the same field of view, and exhibits the evolution of positive (white) and negative (black) magnetic fluxes in the concerned AR. All the features are highlighted in the corresponding channels. Each AIA image contains 480 × 360 pixels, which corresponds to 288 × 216 arcsecs.

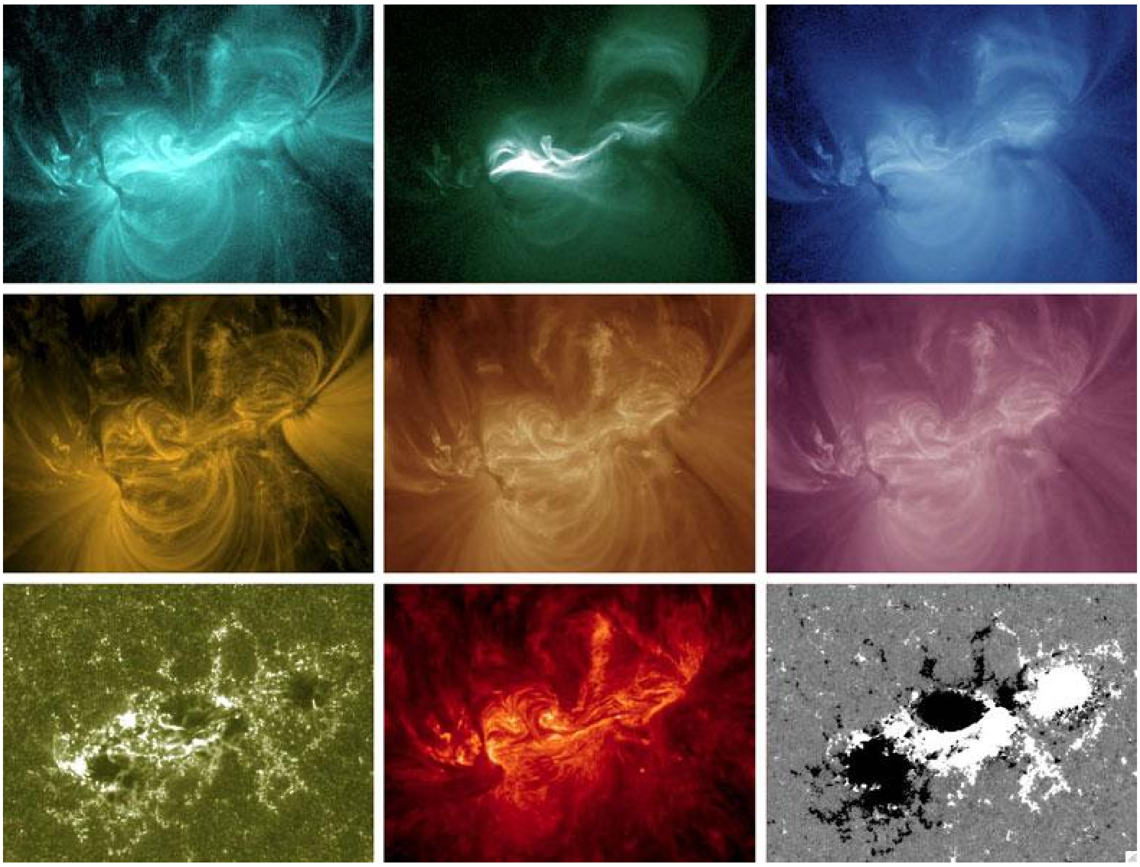

Figure 2.3: Zoomed in view of an active region in different channels of AIA onboard SDO along with the magnetic polarities at their base shown by HMI. (Courtesy: Lemen et al., 2012)

Helioseismic and Magnetic Imager (HMI)

HMI is one of the three instruments onboard SDO which has various capabilities to study the magnetic field at the solar surface (Scherrer et al., 2012). Fe I 6173 Å absorption line (Norton et al., 2006) helps to measure the Doppler shift, line-of-sight magnetic field, intensity, and vector magnetic field at the solar photosphere. Thus, it provides four main types of data: Dopplergrams (maps of solar surface velocity), continuum filtergrams (broad-wavelength photographs of the solar photosphere), and both line-of-sight and vector magnetograms (maps of the photospheric magnetic field). HMI provides full-disk images of the Sun corresponding to 4096 × 4096 pixel CCD camera. The Dopplergram uses the Doppler shift measured by Fe I 6173 Å spectral line inferring photospheric surface velocity with a two-pixel resolution of 1" every 45 seconds. The LOS (line-of-sight) and vector magnetograms both also exploit Fe I 6173 Å spectral line to study Zeeman effect measuring Stokes parameters, which determine longitudinal as well as other vector components of the photospheric magnetic fields. The LOS magnetograms have a temporal cadence of 45 seconds with a two-pixel resolution of 1” while the vector magnetograms have a 12-minute cadence (cf., bottom-right panel in Fig. 2.3).

This instrument is thus mainly used to study the LOS components of magnetic field and related flux variations in time in our work related to the supersonic plasma flow/jet (Chapter 6). Moreover, HMI magnetograms have also helped us in determining the footpoints and related magnetic fields of various cool and hot loop systems studied in Chapters 3-5. However, the instrument has a broad range of utilization to enhance the understanding of solar variability and the Sun’s interior. The LOS magnetograms show the emergence of magnetic field polarities at the solar surface from its inside, which are closely related to eruptive events. The emergence of new magnetic fields and then interacting with existing fields gives rise the studies on a variety of transient and eruptive processes in the solar

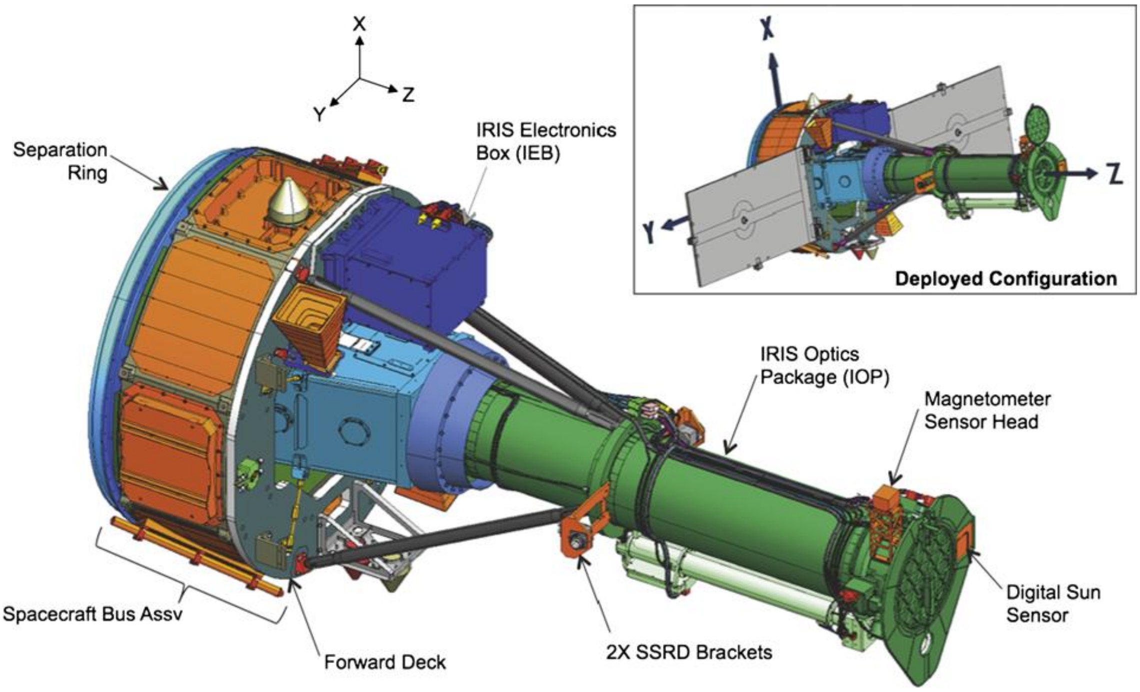

Figure 2.4: Schematic view of IRIS instruments with the telescope from which light is fed into the spectrograph box. (Courtesy: IRIS, LMSAL, NASA)

atmosphere. So, HMI observations lead to linking the physical processes to the dynamics happening in the Sun's atmosphere at chromospheric and coronal levels.

2.2.2 Interface Region Imaging Spectrograph (IRIS)

Interface Region Imaging Spectrograph (De Pontieu et al., 2014a) is a small NASA explorer instrument (cf., Fig.2.4) launched on 27 June 2013 and placed into Sun-synchronous orbit. It has 19-cm UV telescope having slit-based dual-bandpass system of imaging spectrograph mainly focusing on the chromosphere and transition region (TR) which forms a complex interface region between the solar surface (photosphere) and outer atmosphere (corona). It has two instruments for different functions: imaging and spectral data. It works in such a way that the sunlight enters the telescope and falls on the prism having reflective coating and 0.3" × 175" long slit. The reflective coating then directs the light to the slit-jaw imager,

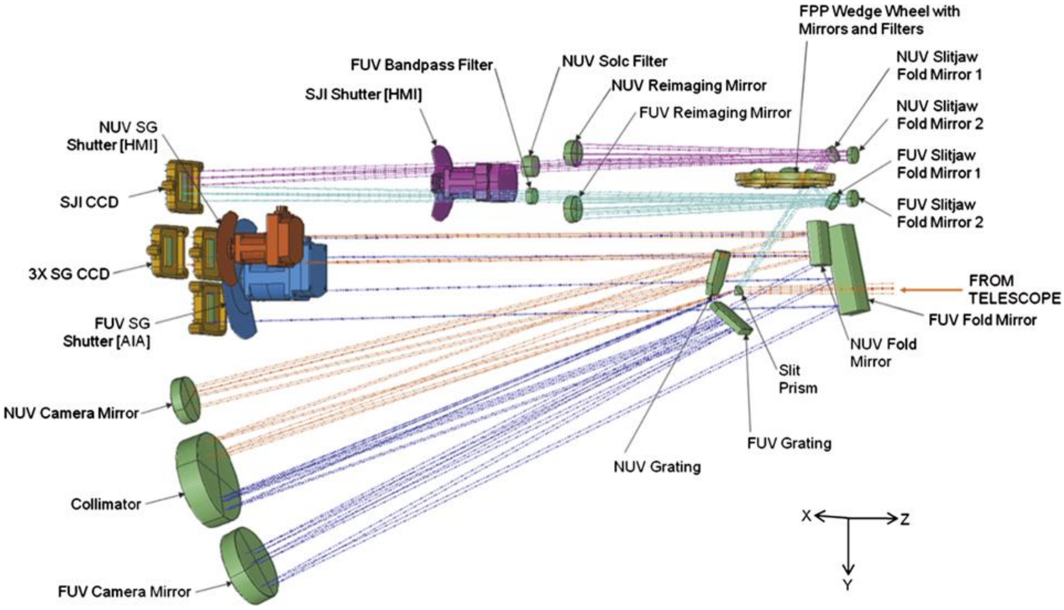

Figure 2.5: Schematic view of the path taken by light in the IRIS spectrograph and slit-jaw imager. (Courtesy: IRIS, LMSAL, NASA)

and the line passing through the slit gets dispersed and directs the light on to the collimator mirror. The dispersed light splits into two different components, i.e., FUV (far ultraviolet) light in the 1332 Å -1407 Å range and NUV (near ultraviolet) light in the 2783 Å -2835 Å range. These FUV and NUV spectrograph beams are then fed to different gratings and mapped onto separate CCDs. The path followed by the light is thus shown in Fig.2.5 by different colors. The dark blue indicates FUV spectrograph light; orange for NUV spectrograph; and purple for NUV slit-jaw. Following this mechanism, orientation of secondary mirror is changed to scan the solar surface and get IRIS raster observations. Fig.2.6 illustrates the solar atmosphere targeting NOAA AR 11817 as observed by IRIS on 14 August 2013 at 18:50 UT. The upper panel shows the IRIS slit-jaw images (SJI) of 2830 Å (Mg II h), 2796 Å (Mg II k), 1330 Å (C II) and 1400 Å (Si IV) at formation temperatures of 6000 K, 15000 K, 30000 and 80000 K, respectively. These spectral lines correspond to different heights of their formation covering near photosphere upto the transition region (TR). The middle row shows the spectrum for two spectral domains: FUV-1 (left) and

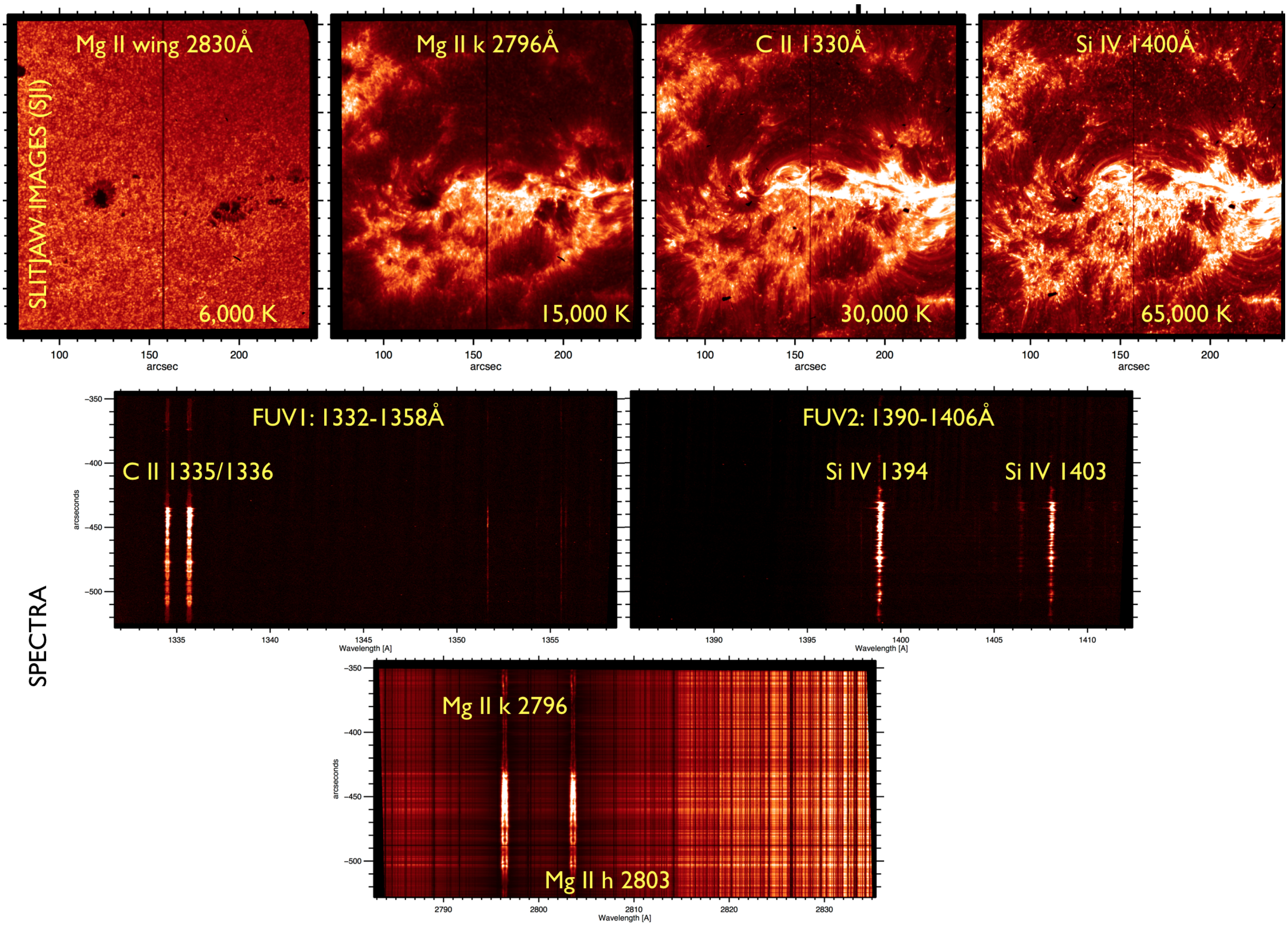

Figure 2.6: The solar atmosphere as observed by IRIS in different wavelength bands. (Courtesy: https://iris.lmsal.com/itn51/iris_data.html)

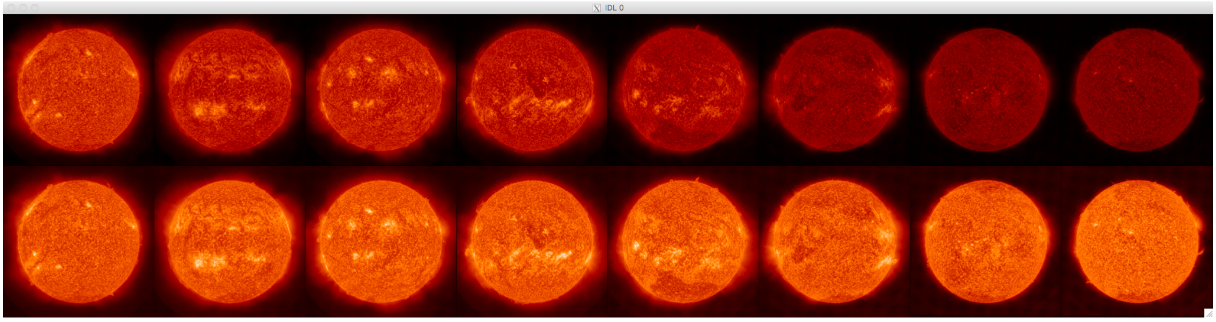

Figure 2.7: From left to right, annual images from the 304 Å channel taken between 2011 and 2018 are displayed, before (top row) and after (bottom row) correcting for changes in the instrument sensitivity. It should be noted that top and bottom rows of the EUV images are already corrected for other artefacts using aia_prep. (Courtesy: LMSAL, NASA, SDO/AIA)

FUV-2 (right). FUV-1 has two strongest lines around 1334 Å -1336 Å formed in the upper chromosphere and low transition region. FUV-2 consist of strongest Si IV line formed in the transition region. The lower row depicts the spectrum of NUV domain exhibiting the Mg II k 2796 Å and Mg II h 2803 Å lines, both formed over a range of heights from the upper photosphere to the upper chromosphere. It also contains many wavelength ranges of photospheric lines. The dark vertical line in the middle of SJI images is the location of the slit while the thin horizontal lines in the spectral data are fiducial marks used for co-alignment of the data.

IRIS allows to bridge the gap between earlier missions which had spectral lines focused in the corona. By exploiting the spectral data from chromosphere and transition region through IRIS observations, we get better insights into the modes of non-thermal energy powering the solar atmosphere and solar wind apart from other broad scientific objectives. However, we may also pursue the studies related to the spectroscopic diagnostics of the plasma giving physical information like velocity, turbulence, non-thermal energy, or density. In the present thesis, we use the IRIS observations to understand the flow structure of the plasma in cool as well as hot loops.

2.3 Data Analysis Techniques

The extraction of physical information from the data obtained from the instruments mentioned in the previous section makes use of the different data analysis techniques. These techniques then help us gaining information about the physical conditions in the solar atmosphere, and are explained briefly.

2.3.1 Image calibration and processing

The imaging data we get from SDO and IRIS is used to analyze to understand the dynamical plasma processes in the solar atmosphere. The raw images obtained from the CCD are flat-fielded, rebinned, processed to remove bad pixels and spikes. These processed images in the form of Level 1.5 (in the form of physical observable) fits file are then used for scientific analysis. The characteristics such as number of pixels in each direction, pixel size, center coordinates are stored in the form of keywords. Using these keywords, the co-alignment of one or more images is done using their image calibration routines (e.g., aia_prep.pro for SDO/AIA). It updates these keywords of all the images corresponding to the reference image according to which all the images are aligned. It also helps us align images from different instruments having different spatial resolution. These images are then enhanced by performing various operations on them (cf., Fig. 2.7). It can be resized according to our interests, manipulated and color contrasted for better understanding of the data. These image processed data are then subjected to various analysis techniques mentioned later in this chapter to get scientific results out of it.

2.3.2 Analysis techniques of magnetogram data

The LOS magnetograms are generally operated through same imaging processes as AIA or IRIS images. However, it exhibits some issues with the instrumental characteristics

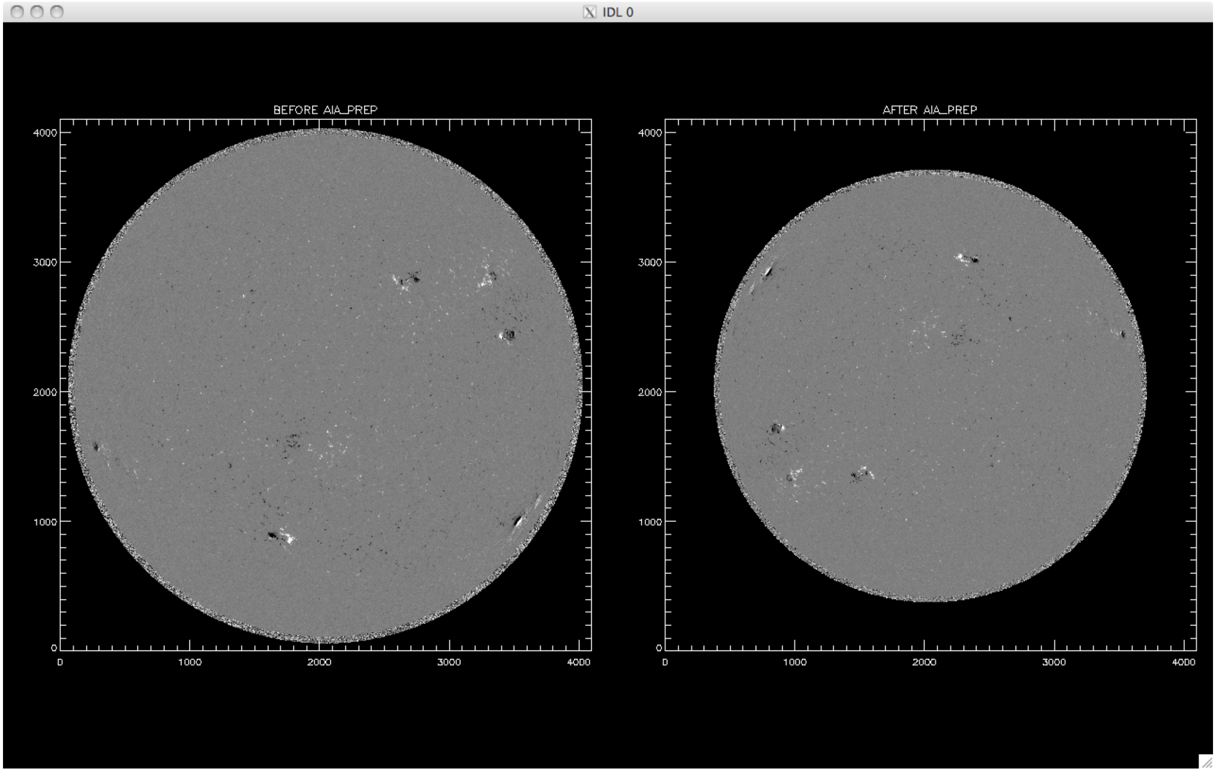

Figure 2.8: The HMI magnetogram images before (left-panel) and after (right-panel) image calibration. (Courtesy: LMSAL, NASA, SDO/AIA)

such as spatial resolution, scattered light, and filter characteristics due to the inherent complexity of the solar magnetic field in space and time. The images are rotated and processed through hmi_prep.pro inbuilt routine (cf., Fig. 2.8). Even though the images are stabilized against spacecraft jitter by an Image Stabilization System (ISS) already, they are manually calibrated and aligned with the reference image from 1600 Å channel of AIA for better co-alignment. The vector magnetograms giving three different components (field strength B_r, inclination B_θ, and azimuth B_ϕ) of the magnetic field generally used for extrapolations is inverted to get physical information. This inversion causes the data to suffer from additional 180-degree ambiguity in the azimuthal field direction. It is first resolved using three methods: the potential-field method, the radial acute-angle method, and the random method and then subjected to scientific techniques for the results.

2.3.3 Spectral analysis

The IRIS spectral data utilized in this thesis (cf., Chapters 3-5) are of three different kinds: Optically thick emission line; optically thin emission line; absorption line. Si IV is an optically thin line which is characterized by single peak profile; Mg II k and C II are optically thick lines generally characterized by double or more peak profiles; Ni I is an absorption line and characterized by inverse Gaussian profile. These lines are then fitted accordingly. We use an iris inbuilt routine (i.e., iris_orbitvarr_corr_l2.pro) to remove the orbital variations before applying the fitting procedure. The estimation of rest wavelengths is very crucial for the estimation of Doppler velocities. We have estimated the observed wavelengths of neutral lines in the very quiet area (Ni I 2799.474 Å and S I 1401.50 Å). Using the shift of the neutral lines, we have estimated the rest wavelengths of Ni I 2799.474 Å, Mg II k 2796.35 Åand Si IV 1402.77 Å. To derive the basic parameters of the line profiles, we use Gaussian fitting to lines of Ni I; formation temperature: log(T/K)

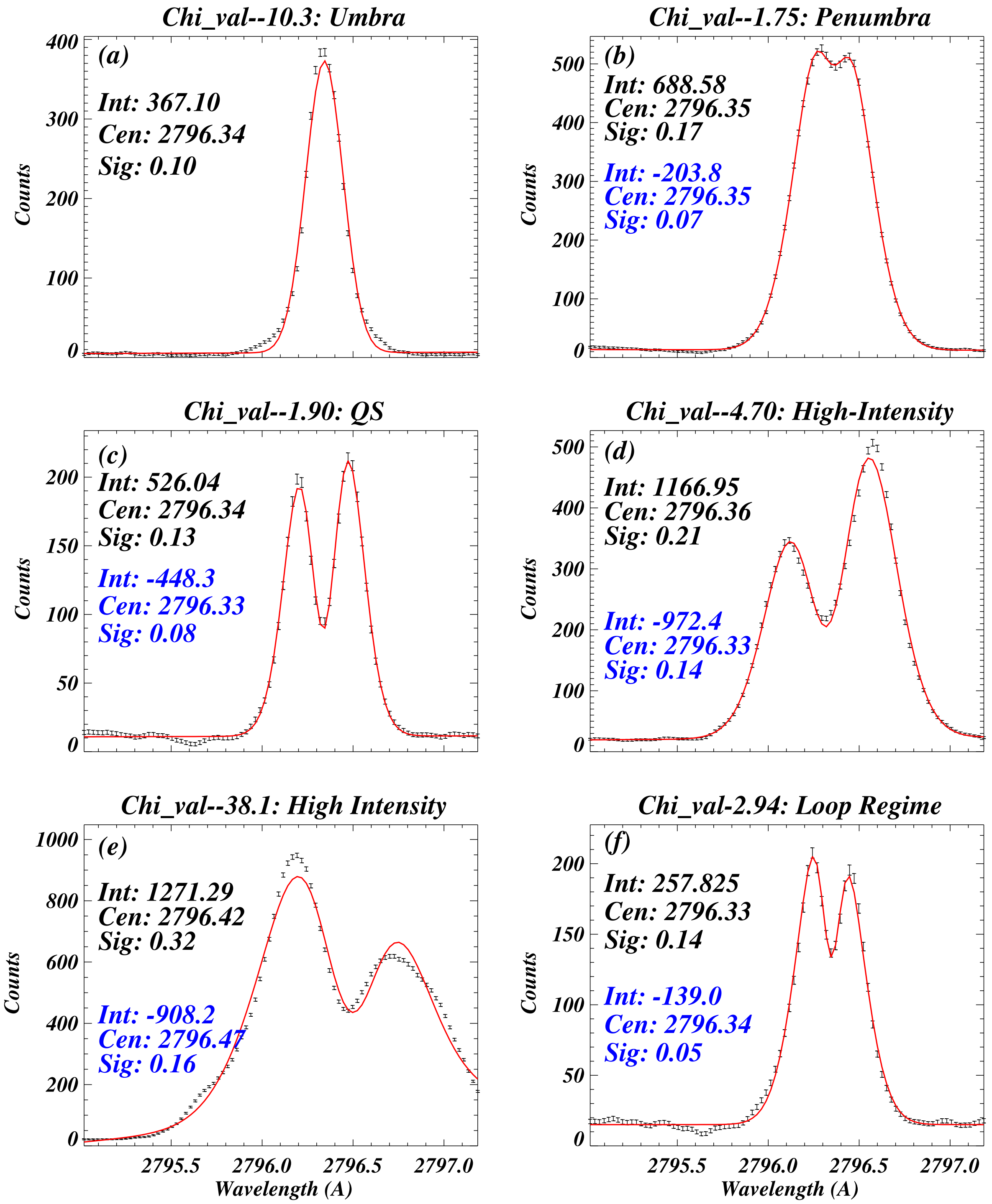

Figure 2.9: Few samples of our fitting model on the observed profiles of Mg II k 2796.35 Å within the different features, e.g., umbra (panel a), penumbra (panel b), QS (panel c), high-intensity (panel d & e) and loop regime (panel f). The black shows the observed profiles while the red line is fitted model on the observed profiles. We have also displayed the parameters (peak intensity, centriod and Gaussian sigma) from positive Gaussian (black) and negative Gaussian (blue) in each panel. These samples illustrates the variations of Mg II k line within the different features in the observed region. The fitting model capture the line behaviour very well, which justify our fitting model for Mg II k line.

= 4.2 (Stucki et al., 2000), Mg II k (2796.20 Å; log (T/K) = 4.0), C II (1334.53 Å; log(T/K) = 4.3), and Si IV (1402.77 Å; log(T/K) = 4.8).

We have performed single Gaussian fitting to the Si IV line, inverse Gaussian fitting to the Ni I lines, and single or double Gaussian fitting, depending on the nature of observed profiles. Since Mg II k lines are optically thick, they provide double Gaussian profiles at most of the locations except for sunspots (Leenaarts et al., 2013; Morrill et al., 2001; Rathore et al., 2015). Mg II k 2796.35 Å and C II 1334.53 Å are optically thick spectral lines (cf, Fig 2.9), which can have single or double peaks or even more (Leenaarts et al., 2013; Rathore et al., 2015). In our observations, we have generally found that a major fraction of of Mg II k 2796.35 Å has double peak profiles (i.e., k2v and k2r) with associated minimum between these two peaks (i.e., k3). However, in case of sunspot umbra the Mg II k are single peak profiles as reported by Tian et al. (2014b). We have used two Gaussian (one positive and another negative) along the straight line to fit the Mg II k 2796.35 Å line. We use the similar fitting model as the one used by Schmit et al. (2015). We have used straight line to fit the continuum while Schmit et al. (2015) have used a polynomial. The same approach is adopted for the C II line.

We have used negative Gaussian for the estimation of Doppler velocity and FWHM for these optically thick lines. In this fitting model, the negative Gaussian basically captures the dip region in between two peaks. The dip-region is formed higher up in the chromosphere (Leenaarts et al. 2013; Rathore et al. 2015). As already noted, these optically thick lines can also have single peak profiles (specifically,C II 1334.532 Å line), Therefore, we do not have the negative Gaussian parameters there. So, the parameters from single Gaussian (as profiles is single peak) are used at those locations to create the corresponding intensity, Doppler velocity and FWHM maps. The developed fitting model is employed to optically thick (examples are shown in Fig. 2.9) and optically thin line-profiles extracted from multiple data sets of IRIS spectroscopic measurements to study the dynamics of cool loop systems (cf., Chapters 3-5).

2.3.4 Differential Emission Measure (DEM) analysis

In order to extract physical information such as density and temperature from the images of the Sun, Differential Emission Measure (DEM) technique is used. It is a technique which measures the amount of plasma along the line-of-sight which contributes to the emitted radiation in the temperature range between T and T+dT (Craig & Brown, 1976):

$$\frac{dEM(T)}{dT} = n_e n_H \frac{dz}{dt} (cm^{-5} K^{-1}) \tag{2.1}$$

and thus, the intensity of a spectral line can be expressed as-

$$I(\lambda_{ij}) = A_\alpha \int_T C(T, \lambda_{ij}, n_e) \tfrac{dEM(T)}{dT} dT (ergs\ cm^{-2}\ s^{-1}\ ster^{-1}),$$

where density profile of the source n(z) = n_e(z) ≈ n_H(z) along LOS in a particular temperature range where A_α is the atomic abundance in the source. C(T,λ_{ij},n_e) is the contribution function including atomic parameters. For given input parameters such as line intensities I(λ_{ij}) and wavelength λ_{ij}, and predefined elemental abundances A_α, the CHIANTI spectral code calculates the contribution function for each transition. The solution of

$$\tfrac{dEM(T)}{dT} = \int_T n_e n_I dz \approx \mathrm{n}_e^2$$

gives the amount of squared density n_e^2 multiplied with the depth 'z' of the source along line-of-sight.

In the above paragraph, a general physical notion of DEM is outlined. Specifically in our work, we have used the method of Hannah & Kontar (2012) to measure the differential emissions from the quiet Sun region where supersonic jet is originated (cf., Chapter 6 for details), and the coronal loops in the moss region (cf., Chapter 5). There are different

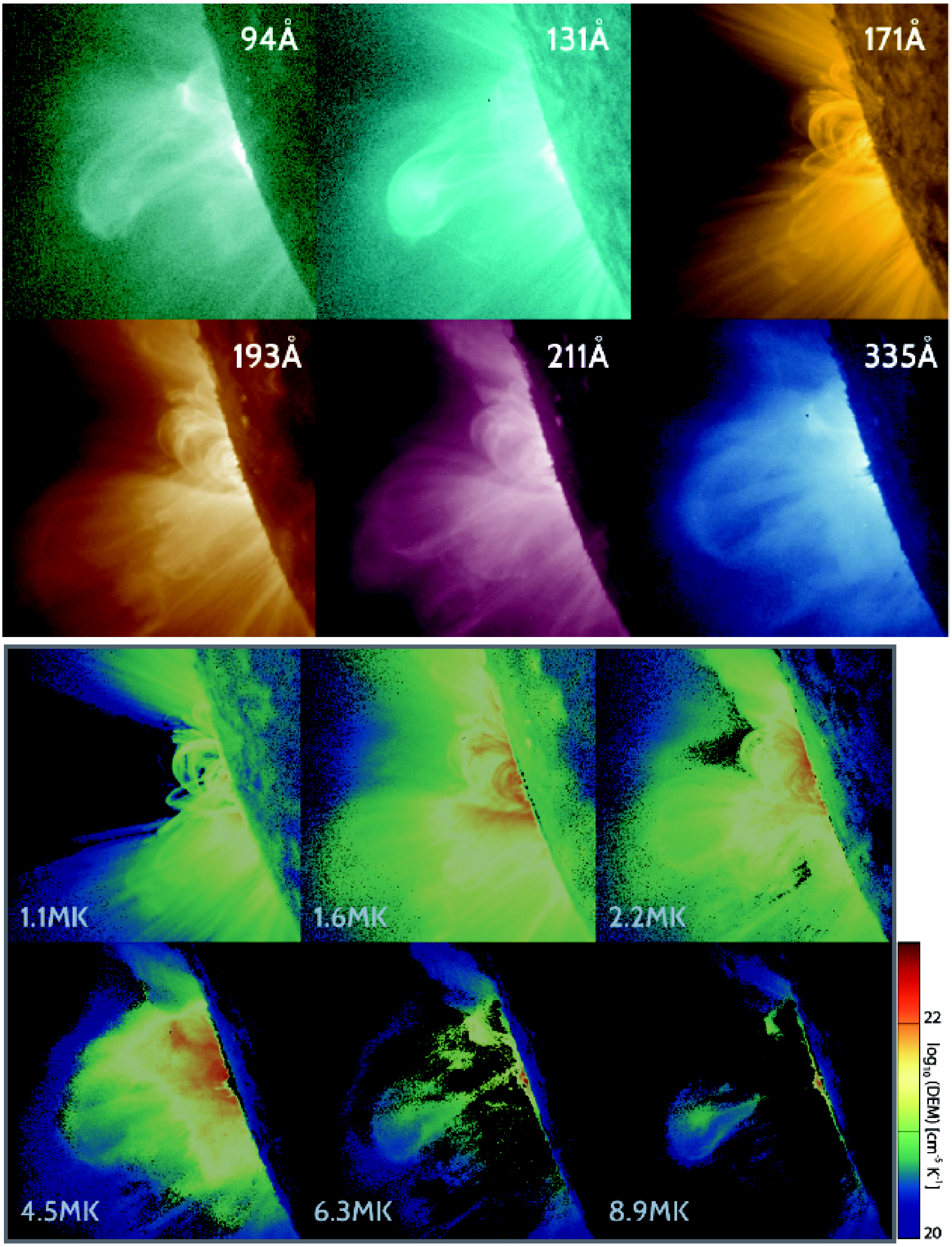

Figure 2.10: Left-panel: SDO/AIA images during C4.9 flare from 03-Nov-2010 at 12:14:36 UT. Right-panel: DEM maps at different temperature produced by regularized inversion method of Hannah and Kontar (2012). The colour scales in bottom mosaic represents DEM value for each temperature range. The hot erupting material is clearly visible in the 8.9MK map. (Courtesy: Ian G. Hannah and E. Kontar)

mathematical methods to solve these equations and produce DEM maps. Hannah & Kontar (2012) used enhanced regularization algorithm to find the line-of-sight DEM. In brief, the total emission measure from the given temperature interval is EM$_T$=DEM(T)dT=$\int_T n_e^2 dz$, which indicates the amount of plasma integrated along the LOS (dz) over per unit area (Mishra et al., 2018). Here, n_e is an electron number density associated with temperature bin size T(K). The used method is an automated method that returns a regularized DEM as a function of temperature (T). For the inversion, it uses zeroth-order regularization in the prescribed temperature range with appropriate bin size. For the given six AIA filters, one can obtain the DEM for the region of interest (ROI) in the selected temperature regions (cf., details of eruptive region in Fig. 2.10). The details of the mathematical model of the mentioned regularization method to obtain DEM is given by Hannah & Kontar (2012).

2.3.5 Time series analysis: A brief description of wavelet

The time analysis is performed using technique Wavelet Analysis which is used to analyze the quasi-periodic signals. Fourier analysis requires a Fourier transform and is used to provide information on the dominant frequencies. However, wavelet analysis requires wavelet transform and has an added advantage of providing the time localization of the various frequency components. So, it allows the frequency as well as temporal information of any periods present within data to be analyzed. Torrence & Compo (1998) gives detailed description about wavelet transform and wavelet analysis. However, the method can be briefly summarized by assuming time series x$_N$ of N observations and constant sample spacing δt, the wavelet transform is defined as the convolution of x$_N$ with a scaled and translated wavelet (or mother function) ψ_η where η is the non-dimensional time parameter. Acceptable wavelet functions are localized in time and frequency space with zero mean, thus we assume ψ to be normalized, i.e

$$\int_{-\infty}^{\infty} \psi\psi^* d\eta = 1$$

The continuous wavelet transform is defined as-

$$W_n(s) = \sum_{n'=0}^{N-1} x_{n'} \sqrt{\frac{\delta t}{s}} \psi^* [\frac{(n'-n)\delta t}{s}] \tag{2.2}$$

where $\eta = \frac{(n'-n)\delta t}{s}$ is the wavelet scale and n allows the wavelet function to be translated in time. So, a 2D power spectrum is formed by varying the wavelet scale 's' and translating along time index n. This shows the variation of periods as a function of time and scale. The $|\mathrm{W}_n(\mathrm{s})|^2$ defines the wavelet power spectrum. However, the finiteness of time-series and wavelet function causes the edge effects at the ends of time series proportional to the scale. Thus, a cone of influence (COI) is defined as a region where wavelet power drops by a factor of e^{-2} where edge effects are hard to neglect. The wavelet power spectrum outside COI is then not considered for our analysis due to edge effects. Another parameter which determines the quality of wavelet analysis is significance level on any periods present in the wavelet power spectrum. A background noise spectrum is assumed and then compared with the data power spectrum (Ireland et al., 1999). Significance contours are formed inside which wavelet power can be considered as being real within a given confidence level. However, in our wavelet software, we utilize the randomization technique to estimate the significance levels. It obtains measurements of the peak power in the global wavelet spectrum, which is the average peak power over time, and is equivalent to a smoothed Fourier power spectrum. The probability measurements of the real power peaks have been carried out by the randomization test (O'Shea et al., 2001). This technique parametrically estimates the fraction of permutations that provide peak values greater than or equal to the original peak power of the time series, which provides the probability (p) of the null periodic component. Thus, the acceptance percentage probability that real periodic components are present in the data is $(1-p)\times 100$. The details of the randomization test

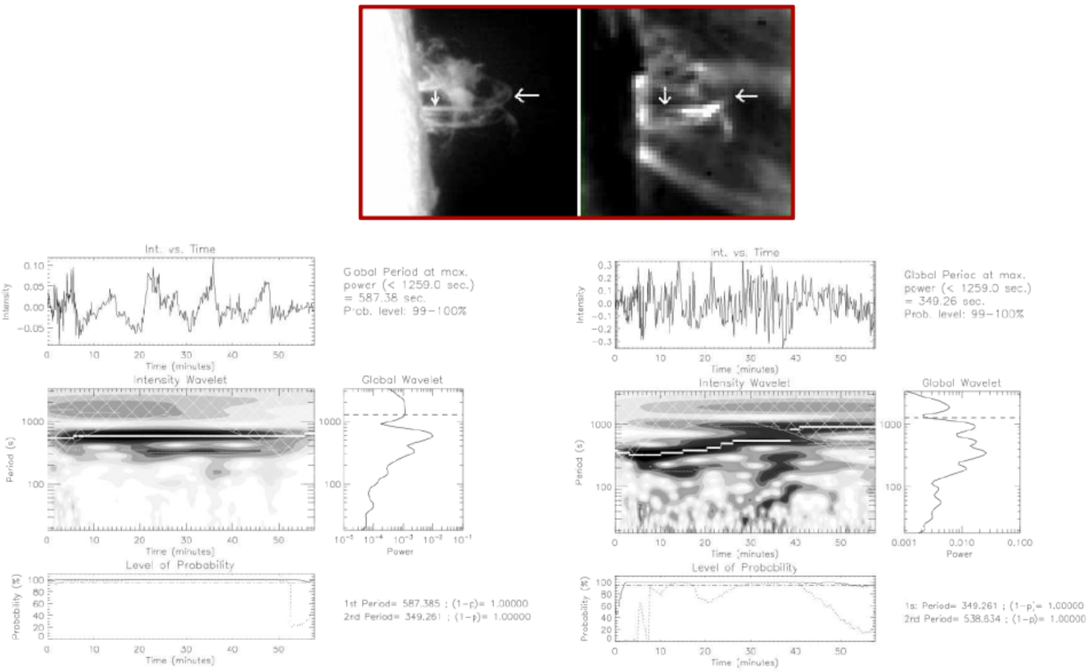

Figure 2.11: Example of a wavelet analysis: The multiple harmonics of the sausage oscillations are firstly detected in cool loop system in the solar atmosphere. Top-left image is observed by 15-cm ARIES Solar Tower Telescope in Hα, while top-right is the aligned image panel as observed by SoHO/EIT in Fe IX/FeX 171 Å line. This case study demonstrates the use of wavelet as a powerful tool to derive novel scientific results. The top panel in each wavelet diagram shows the original light curves derived from the cool loop system. The middle-left panels display the intensity wavelet with the COI region in form of cross-hatched area, while the middle-right panels represent global wavelet power. The bottom most panels represent the variation of the probability. (Courtesy:- Srivastava et al., 2008)

are given by Linnell Nemec & Nemec (1985). Such a powerful tool is utilized to devise a variety of novel scientific discoveries in the field of solar physics. One example is depicted in Fig. 2.11 where it is shown that significant periodicities are derived associated with the multiple sausage wave harmonics in cool loop system for the first time (Srivastava et al., 2008). In the present thesis, the wavelet analysis with randomization test is utilized in Chapter 6 in order to obtain the signature of the oscillatory processes at the base of supersonic jet in the HMI magnetic and AIA 1600 Å fluxes.

2.4 Conclusions

In conclusion, these various techniques are employed to extract physical conditions of the plasma using imaging and spectral observation from different instruments as mentioned in this chapter. Thus, the dynamics of the complex interactions between magnetic fields and plasma are studied with scientific interpretation of the information resulting from our analysis. These phenomena are coupled in the different atmospheric layers and most likely carry mass and energy to the outer atmosphere. We will study the plausible physical mechanisms responsible to give rise to such phenomena in the following chapters of the thesis. In chapter 3, we describe the multi-wavelength and multi-spectral studies related to the plasma flows above the footpoints of the cool loop systems.